Available online at www.sciencedirect.com
ScienceDirect
Trans. Nonferrous Met. Soc. China 35(2025) 1603−1618
Transactions of Nonferrous Metals Society of China
www.tnmsc.cn

Effect of rejuvenation heat treatment on serrated flow behavior and fracture mechanism of nickel-based superalloys

Jia-jian WANG[1], Zhe-wen HAN[2], Zhi-chun WANG[2], Bo PENG[2], Yue ZUO[3], Ju KANG[1,4,5]

1. School of Mechanical Engineering, Beijing Institute of Petrochemical Technology, Beijing 102617, China;
2. North China Electric Power Research Institute Co., Ltd., Beijing 100045, China;
3. Welding Institute, Central Iron & Steel Research Institute, Beijing 100081, China;
4. Hydrogen Energy Research Centre, Beijing Institute of Petrochemical Technology, Beijing 102617, China;
5. State Key Laboratory of Tribology in Advanced Equipment, Tsinghua University, Beijing 100084, China

Received 14 October 2023; accepted 3 June 2024

Abstract: The effects of rejuvenation heat treatment (RHT) on the serrated flow behavior and fracture mode of nickel-based superalloys (R26) were investigated by tensile tests and microstructural characterization. The serrated flow activation energies were determined to be 41−72 and 64−81 kJ/mol before and after RHT, respectively. Dynamic strain aging in the alloy is caused by the diffusion of carbon atoms into dislocation channels in the nickel matrix. Before RHT, carbides are concentrated at the grain boundaries. Cracks initiate from these carbides and propagate along the grain boundaries. RHT dissolves carbides at grain boundaries, transferring crack initiation to the precipitated phase group in the grains. RHT increases carbon atom concentration in the nickel matrix, enhancing dynamic strain aging and serrated flow behavior.
Key words: rejuvenation heat treatment; nickel-based superalloy; serrated flow behavior; fracture; activation energy

1 Introduction

Ni-based alloys have excellent fatigue and creep resistance in high-temperature environments and have been widely used in fields such as the aerospace and gas turbine manufacturing industries [1−3]. High-temperature bolts made of Ni-based alloys directly affect the safety of nuclear, thermal, and other power plant units [4,5]. High-temperature bolts operating in harsh environments for extended periods are often subjected to high temperatures and complex loads, which can lead to gradual material degradation or fracture [6,7].

The deformation mechanism of Ni-based superalloys is primarily determined by dislocation slip or twinning, and these alloys exhibit plastic instability over a wide range of temperatures and tensile rates. A typical phenomenon is serrated flow on the stretching curve [8], which is usually called the Portevin-Le Chatelier (PLC) effect. The PLC effect is observed in many alloys and is closely related to their mechanical properties and fracture modes [9−11]. The PLC effect is generally considered to be the result of the interaction between moving dislocations and the solute atmosphere or shear precipitates. This process of pinning/unpinning of dislocations by solutes or precipitates causes dynamic strain aging (DSA), resulting in an increase/decrease in tensile stress [12]. The DSA model suggests that solute atoms and dislocation densities play important roles in determining the PLC parameters (stress drop and reloading time) during plastic deformation [12−15]. GENG et al [13] and AIT-AMOKHTAR et al [14] reported that the stress drop increased with the

Corresponding author: Ju KANG, Tel: +86-10-81292139, E-mail: kangju@bipt.edu.cn
https://doi.org/10.1016/S1003-6326(25)66770-7

increase in the Mg content, which made the DSA phenomenon more significant. Thus, precipitates consisting of solute atoms are thought to reduce the PLC effect. The microscopic mechanisms of DSA are controversial. In the solute pipeline diffusion model proposed by SLEESWYK [15], the solute atoms first gather around dislocation forests or precipitates. When a movable dislocation is blocked, solute atoms gather along the dislocation line to the movable dislocation to achieve pinning. After the movable dislocation is unpinned, the solute atoms remain in place and resegregate into dislocation forests or precipitates.

Various studies on serrated flow in alloys have shown that evaluating the activation energy of serrated flow is essential for elucidating solute atoms and their mode of aggregation to movable dislocations in DSA. Interstitial atoms (such as C and N) in alloys are considered to interact with movable dislocations. HAYES et al [16] evaluated the activation energy to determine whether the PLC effect in Waspalloy alloys is a result of the interaction of the carbon solute with mobile dislocations. The occurrence of serrated flow is related to the diffusion energy as well as the solute dislocation binding energy. For example, NALAWADE et al [17] compared the serrated flow behavior of the 718 alloy under different metallurgical conditions, attributed the high-temperature PLC effect to the interaction between Nb and movable dislocations, and excluded the possibility of Mo leading to a high-temperature PLC effect [18]. However, MAX et al [19] found a serrated flow in 718 alloys containing Mo without Nb, which means that Nb cannot be considered as the only reason for the PLC effect of the 718 alloy. Common methods for calculating the activation energy include the Arrhenius, critical strain, McCormick, and serration amplitude methods [19−24]. Since the critical strain and McCormick methods require the evaluation of vacancy concentrations and dislocation densities that are difficult to verify in plastic deformation, QIAN and REED-HILL [25] proposed the intercept method that does not involve the use of $m+\beta$ values (m and β are exponents of the variation of the vacancy concentration and the density of mobile dislocations with plastic strain, respectively).

R26 alloy suffers from excessive hardness, abnormal microstructure and serrated flow after long-term service [26], which causes the alloy to undergo brittle fracture and reduces alloy service life. According to the maintenance specifications of the power station, if the hardness of the R26 bolt does not meet the standard requirements, it must be abandoned. As an alternative to expensive parts, rejuvenation heat treatment (RHT) can effectively adjust the comprehensive mechanical properties of damaged high-temperature bolts [27,28]. The PLC effect is generally considered to negatively affect alloys [24,29]. Therefore, it is important to study the PLC effect of alloys after RHT. In a previous study [30], we repaired the organization of R26 alloy after service using RHT, which effectively improved the relaxation resistance of the alloy. In the present study, we used RHT to adjust the hardness of R26 high-temperature bolts that had been in service in a power plant. We investigated the solutes and their diffusion modes contributing to the PLC effect in the R26 alloy. The relationship between PLC effect and fracture mechanism was explained by the evolution of the solute and the corresponding precipitated phase, and the influence of RHT on the microstructure, fracture mode, and serrated flow of the R26 superalloy. The findings of this study provide a theoretical reference for the recovery of high-temperature alloy properties after service, and help to design new alloys with life regeneration potential.

2 Experimental

2.1 Materials and rejuvenation heat treatment process

Two R26 superalloy bolts (numbered 1# and 2#), with size 25 mm × 272 mm, which had failed the Brinell hardness test after being in service for over 6×10^4 h, were used as the test material. The chemical composition of the R26 superalloy (Table 1) was analyzed using a benchtop spectrometer (Oxford FOUNDRY MASTER PRO).

RHT was performed on Bolt 1# to repair its performance, whereas Bolt 2# did not undergo RHT. The RHT process is shown in Table 2. The first step was pre-heat treatment (1200 °C/h to 815 °C, holding for 4 h, followed by furnace cooling), and the second step was aging treatment (1200 °C/h to 730 °C, holding for 4 h, followed by air cooling). Following the GB/T 228.2—2015 standard, the tensile samples were obtained by

cutting the middle part of R26 superalloy bolts; the sampling position is shown in Fig. 1(a). The dimensions of the tensile specimens are shown in Fig. 1(c).

Table 1 Chemical composition of R26 superalloy (wt.%)

C	Si	Mn	Mo	Ti	Cr	Co	Fe	Ni
0.05	0.06	0.22	2.86	2.88	17.60	18.30	21.48	Bal.

Table 2 Parameters of RHT process

Step	Heat treatment process	Heating rate/ (°C·h^{-1})	Holding temperature/ °C	Holding time/ h	Cooling type
1	Preheating	1200	815	4	Furnace cooling
2	Aging	1200	730	4	Air cooling

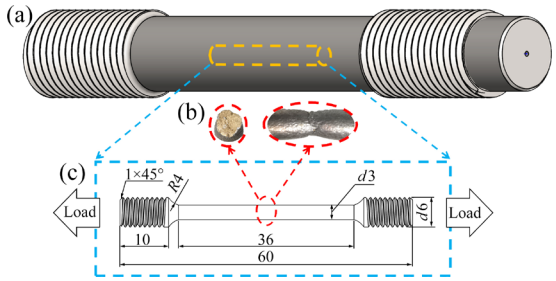

Fig. 1 Schematic diagrams of tensile specimen preparation: (a) Sampling position of R26 superalloy bolt and tensile specimen; (b) Tensile fracture and necking morphology; (c) Size of tensile specimen (unit: mm)

2.2 Tensile tests

Following the GB/T 228.2—2015 standard, axial tensile tests were performed on the tensile specimens (as shown in Fig. 1(c)) using a tensile testing machine (ETM−105D microcomputer-controlled electronic universal testing machine). In order to calculate the activation energy, a series of tensile tests were performed at different temperatures and strain rates [21,31]. The parameters of the tensile tests are shown in Table 3, and the tensile tests were conducted at four temperatures: 260, 360, 460 and 560 °C. Tensile tests with strain rates of 7×10^{-5}, 2.5×10^{-4}, and 1.4×10^{-3} s^{-1} were performed at each temperature, for a total of 12 groups with 3 parallel specimens in each group. The specimens were maintained at the test temperature for 2 min before stretching to ensure uniform heating. Tensile tests were also performed at 23 °C in order to analyze the fracture at room temperature.

Table 3 Parameters of tensile test

Sample	RHT or not	Temperature/°C	Strain rate/s^{-1}
R1/N1	Yes/No	260	7×10^{-5}
R2/N2	Yes/No	260	2.5×10^{-4}
R3/N2	Yes/No	260	1.4×10^{-3}
R4/N4	Yes/No	360	7×10^{-5}
R5/N5	Yes/No	360	2.5×10^{-4}
R6/N6	Yes/No	360	1.4×10^{-3}
R7/N7	Yes/No	460	7×10^{-5}
R8/N8	Yes/No	460	2.5×10^{-4}
R9/N9	Yes/No	460	1.4×10^{-3}
R10/N10	Yes/No	560	7×10^{-5}
R11/N11	Yes/No	560	2.5×10^{-4}
R12/N12	Yes/No	560	1.4×10^{-3}

2.3 Calculation of activation energy

The serrated flow phenomenon was evaluated using tensile tests. To avoid errors in the calculation, various methods are typically used to calculate the activation energy. The three methods were used in this study to calculate the activation energy separately: critical strain model, McCormick method, and the intercept method. The latter does not involve calculating $m+\beta$ and can be used for the validation of the other two methods.

(1) Method 1: Critical strain model

The study of serrated flow shows that the critical strain at the beginning of serration and its dependence on temperature and strain rate can be expressed as [19]

$$\varepsilon_c^{m+\beta}=K\dot{\varepsilon}\exp[Q/(RT)] \quad (1)$$

where Q is the activation energy of the serrated flow; ε_c is the critical strain at the beginning of the serrated flow; $\dot{\varepsilon}$ is the strain rate; K is a constant; R is the molar gas constant (8.314 J/(mol·K)); T is the thermodynamic temperature;

(2) Method II: McCormick method

A quasi-static aging model is commonly used to determine the activation energy, using the following equation [22]:

$$\frac{\varepsilon_c^{m+\beta}}{T}=\exp\left(\frac{Q}{RT}\right)\cdot\left(\frac{C_1}{\phi C_0}\right)^{3/2}\cdot\frac{Rb\dot{\varepsilon}}{LNU_mD_0} \quad (2)$$

where C_l is the local concentration of solute at the dislocation; C_0 is the initial concentration of solute in the alloy; b is the magnitude of Burger's vector; L is the distance between obstacles; U_m is the maximum solute–dislocation interaction energy; D_0 is the frequency factor; N and ϕ are constants.

Rewriting Eqs. (1) and (2) in logarithmic form yields linear Eqs. (3)−(5) in the form $y=ax+b$ [24], where a is the slope of the line. Equation (3) represents a line with coordinate axes $\ln\dot{\varepsilon}$ and $\ln\varepsilon_c$ and slope $m+\beta$. Equation (4) represents a line with coordinate axes $\ln\varepsilon_c$ and $1/T$ and slope $Q/[R(m+\beta)]$. Equation (5) represents a line with coordinate axes $\ln(\varepsilon_c^{m+\beta}/T)$ and $1/T$ and slope Q/R. From the plots of the three linear functions, the values of the slopes $m+\beta$, $Q/[R(m+\beta)]$, and Q/R can be computed, which in turn allows computing Q.

$$\ln\dot{\varepsilon}=(m+\beta)\ln\varepsilon_c-\left(\ln K+\frac{Q}{RT}\right) \tag{3}$$

$$\ln\varepsilon_c=\frac{Q}{R(m+\beta)}\cdot\frac{1}{T}+\frac{\ln K+\ln\dot{\varepsilon}}{m+\beta} \tag{4}$$

$$\ln\left(\frac{\varepsilon_c^{m+\beta}}{T}\right)=\frac{Q}{R}\cdot\frac{1}{T}+\ln\left[\left(\frac{C_l}{\phi C_0}\right)^{3/2}\frac{Kb}{LNU_mD_0}\dot{\varepsilon}\right] \tag{5}$$

(3) Method III: Intercept method [25]

From the plot of critical strain versus tensile rate at different temperatures, different values of critical strain can be chosen to obtain the corresponding values of tensile rate and temperature, constituting the $\ln\dot{\varepsilon}$ vs $1/T$ graph, and the slope of the line correlates with the activation energy.

2.4 Microstructural characterization

Several small specimens were obtained in the direction perpendicular to the axis of the tensile specimen, and the microstructure was observed using a Quanta 450 FEG scanning electron microscope (SEM) and an FEI Tecnai G^2 F30 transmission electron microscope (TEM). The SEM samples were etched in a solution of 5 g $FeCl_3$ + 50 mL HCl + 100 mL C_2H_5OH for approximately 140 s, followed by rinsing with anhydrous ethanol and blow-drying. The TEM samples were mechanically ground to 40−50 μm, and then ion thinning was performed using a precision ion polishing system (Gatan PIPS) (thinning test parameters were: 10 °C, 6 kV, 1 h; 6 °C, 5 kV, 0.5 h; 3 °C, 3 kV, 0.5 h). Energy dispersive spectroscopy (EDS) and selected area electron diffraction (SAED) accompanying TEM were used to characterize the composition and structure of the precipitated phases.

3 Results

3.1 Mechanical properties

The effect of RHT on the bolts is shown in Table 4. The Brinell hardness of Bolts 1# and 2# before RHT is higher than the requirements of the DL/T 439—2018 standard. RHT reduces the Brinell hardness of Bolt 1# to within the required range.

Table 4 Brinell hardness of alloys before and after RHT

Sample	Average Brinell hardness		Brinell hardness standard (DL/T 439—2018)
	Before RHT	After RHT	
Bolt 1#	373.1	327.2	262−331
Bolt 2#	375.1	−	

Figure 2 shows the stress−strain curves of R26 alloy before and after RHT at different strain rates from 260 to 560 °C. To avoid excessive curve overlap, each subgraph shows only six sets of curves. As shown in Figs. 2(a) and (b), the alloys before RHT did not exhibit a significant yield point and fractured shortly after reaching the maximum tensile stress. In comparison, in Figs. 2(c) and (d), the alloys after RHT underwent a much longer yield phase until fracture. Serration is evident from the stress–strain curve in the temperature range of 260−460 °C. As the alloys exhibit less or later onset serrations at 560 °C, the amount of data is insufficient to support an assessment of the activation energy at this temperature; therefore, the study of the serration activation energy in the following section focuses on the analysis of curves in the temperature range of 260−460 °C.

Figure 3 shows the tensile properties of R26 alloys before and after RHT. The strengths of both sets of specimens are strongly dependent on the temperature and show a similar trend. The maximum tensile strength of R26 alloy occurs at 260 °C and decreases monotonically between 260 and 560 °C. The elongation has a stabilized zone between 260 and 460 °C, and then rises to a maximum at 560 °C. Compared with that of the alloy before RHT, the tensile strength of the alloy

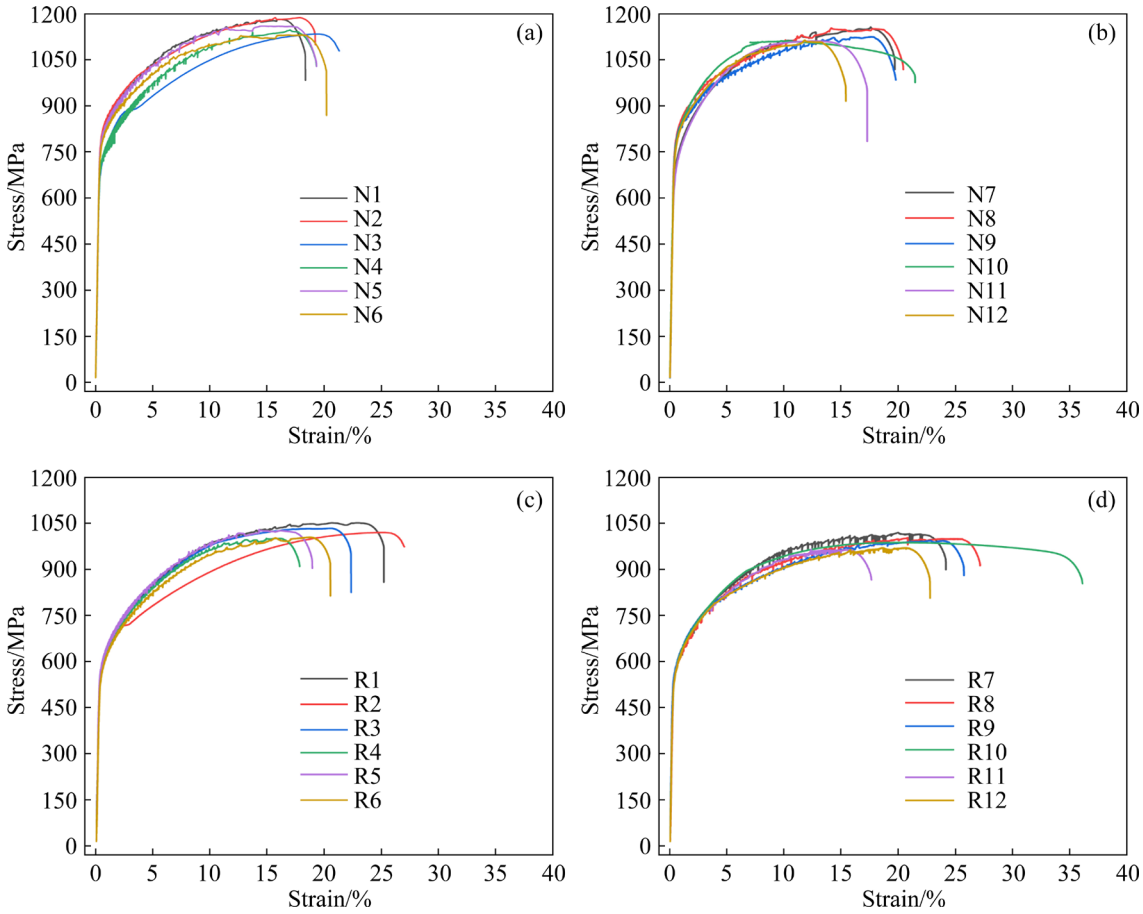

Fig. 2 Stress−strain curves of alloys before (a, b) and after RHT (c, d)

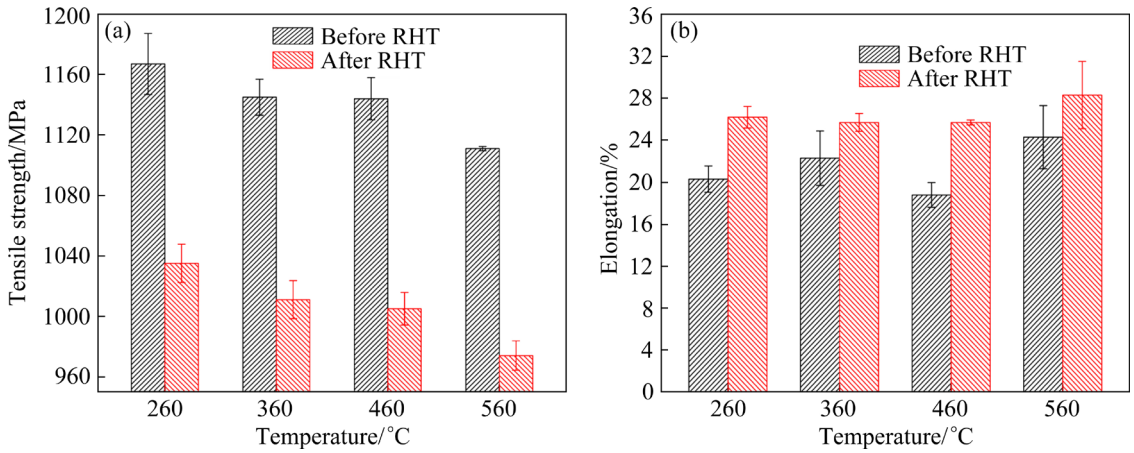

Fig. 3 Tensile properties of R26 alloy before and after RHT: (a) Tensile strength; (b) Elongation

after RHT decreases and the elongation increases, indicating better plasticity.

3.2 Serrated flow behavior and activation energy

Characteristics of the serrations in the stress–strain curve (Fig. 2) are shown in Fig. 4(a). The stress drop ($\Delta\sigma$) of the stress curve is defined as the difference between the maximum stress and the minimum stress of each serration. The reloading time of the serration (Δt) is defined as the time from the minimum stress to the maximum stress of each serration, which reflects the duration of the dislocation locking at the obstacle. These two parameters are used to characterize the occurrence of serrated flow behavior [13]. In this study, the average stress drop and the average reloading time

increase with increasing temperature, as shown in Figs. 4(b) and (c). Compared with the alloy before and after RHT, the stress drop of the alloy after RHT is larger, the reloading time is longer, and the serrated flow behavior is more obvious.

In this study, serrated flow was considered to start when the serrated strain amplitude was greater than 1 MPa. The critical strain represents the strain at the onset of serrated flow, and its value is obtained from Fig. 2. Figure 5 shows the dependence of the critical strain of the alloy on different strain rates and temperatures before and after RHT. From the analysis of Fig. 5(a), with an increase in strain rate, the critical strain increases sharply in the lower strain rate stage ($0–3\times10^{-4}$ s^{-1}), the increase slows down in the higher strain rate stage ($3\times10^{-4}–1.4\times10^{-3}$ s^{-1}), and a stabilization phase ensures. However, at 260 °C, the critical strain still maintains a large increase in the higher strain rate stage. From the analysis of Fig. 5(b), compared with the alloy before RHT, the critical strain of the alloy after RHT maintains a increase with the increase of strain rate at 260 and 360 °C and no clear stabilization phase appears. From the

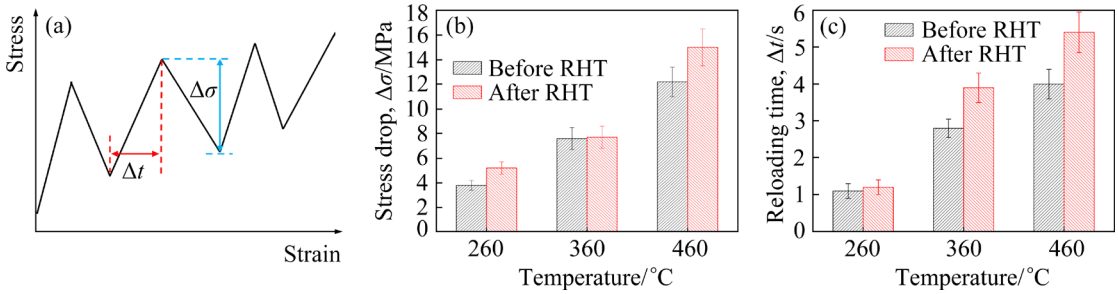

Fig. 4 (a) Definitions of stress drop ($\Delta\sigma$) and reloading time (Δt); (b) Comparison of average stress drop before and after RHT; (c) Comparison of average reloading time before and after RHT

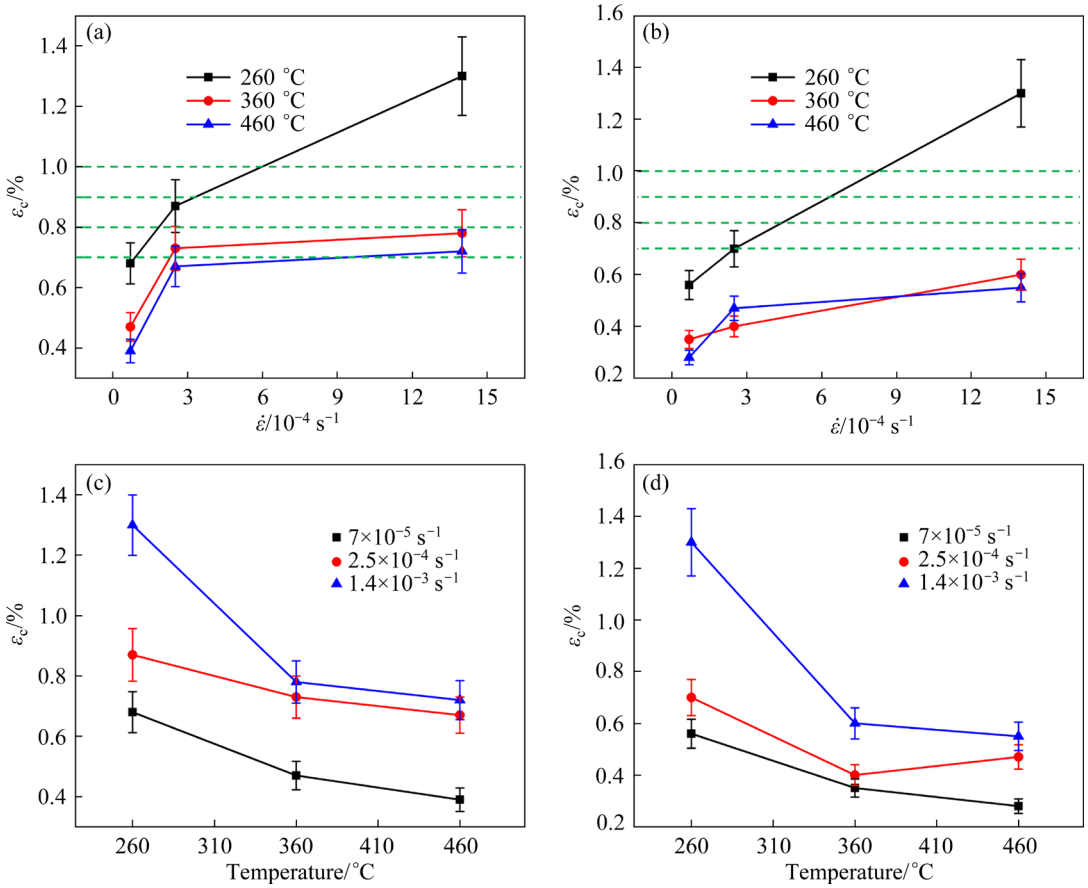

Fig. 5 (a) Critical strain versus strain rate before RHT; (b) Critical strain versus strain rate after RHT; (c) Critical strain versus temperature before RHT; (d) Critical strain versus temperature after RHT

analysis of Figs. 5(c) and (d), the alloy before and after RHT shows a similar change in critical strain with temperature: between 260 and 360 °C, the critical strain decreases significantly with the increase in temperature; between 360 and 460 °C, the critical strain reduction slows down and a stabilization phase occurs.

The $\ln\dot{\varepsilon}$ versus $\ln\varepsilon_c$ plot is shown in Fig. 6, and according to Eq. (3), the slope of the line gives the values of $m+\beta$. The $m+\beta$ values of the alloy before RHT were calculated from Fig. 6(a) at 260, 360, and 460 °C to be 4.3, 4.6, and 3.7, respectively. From Fig. 6(b), the corresponding $m+\beta$ values of the alloy after RHT were calculated to be 2.9, 3.5, and 3.2. $m+\beta$ values can be used to calculate the activation energy.

Method I [19] was used to calculate the activation energy. Figure 7 shows the $\ln\varepsilon_c$ versus $1/T$ plot. According to Eq. (4), the linear slope (n_1) is $Q/[R(m+\beta)]$, that is, $Q=n_1\cdot R\cdot(m+\beta)$. The Q values of the alloys before RHT were calculated from Fig. 7(a) at strain rates of 7×10^{-5}, 2.5×10^{-4}, and 1.4×10^{-3} s^{-1} to be 78, 56, and 81 kJ/mol, respectively. The corresponding Q values of the alloys after RHT were calculated from Fig. 7(b) to be 71, 60, and 90 kJ/mol.

Method II [22] was used to calculate the activation energy. Figure 8 shows the $\ln(\varepsilon_c^{m+\beta}/T)$ vs $1/T$ plot. According to Eq. (5), the linear slope (n_2) is Q/R, that is, $Q=n_2\cdot R$. The Q values of the alloy before RHT were calculated from Fig. 8(a) at strain rates of 7×10^{-5}, 2.5×10^{-4}, and 1.4×10^{-3} s^{-1} to be 61, 41, and 66 kJ/mol, respectively. The corresponding Q values of the alloys after RHT were calculated from Fig. 8(b) to be 63, 51, and 79 kJ/mol.

The activation energy was calculated using Method III [25]. Figure 9 shows the $\ln\dot{\varepsilon}$ versus $1/T$ plot, where $Q=n_3\cdot R$ (n_3 is the slope). The strain rate and temperature corresponding to ε_c values of 0.7%, 0.8%, 0.9%, and 1.0% were obtained by estimating the intersections of the dashed lines in

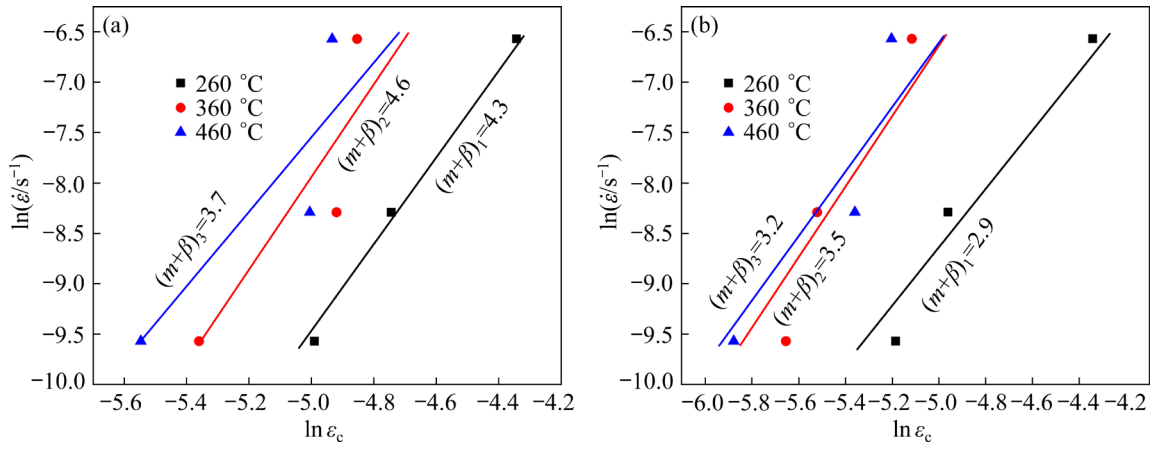

Fig. 6 $\ln\dot{\varepsilon}$ versus $\ln\varepsilon_c$ plots for specimens in different heat treatment states at different temperatures: (a) Before RHT; (b) After RHT

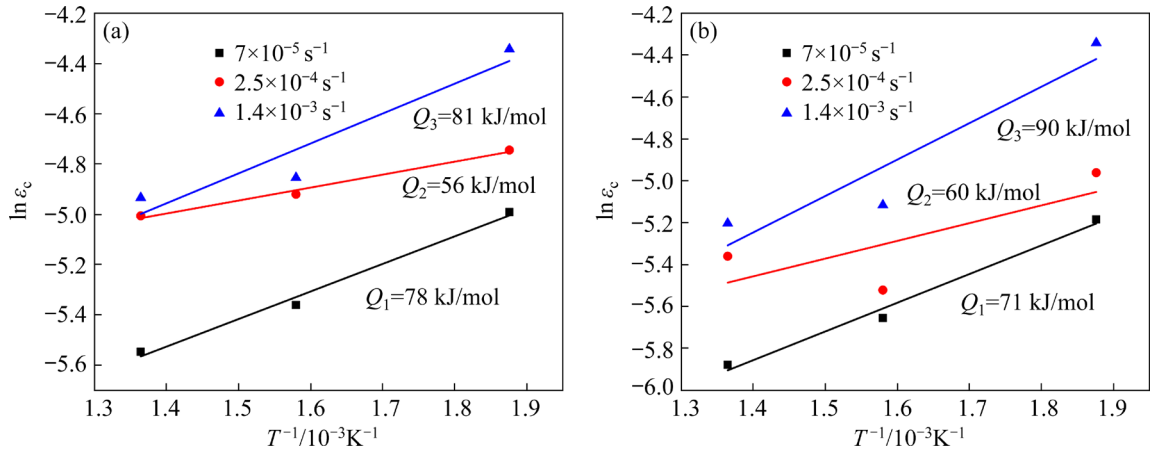

Fig. 7 $\ln\varepsilon_c$ versus $1/T$ plots under different strain rates using Method I: (a) Before RHT; (b) After RHT

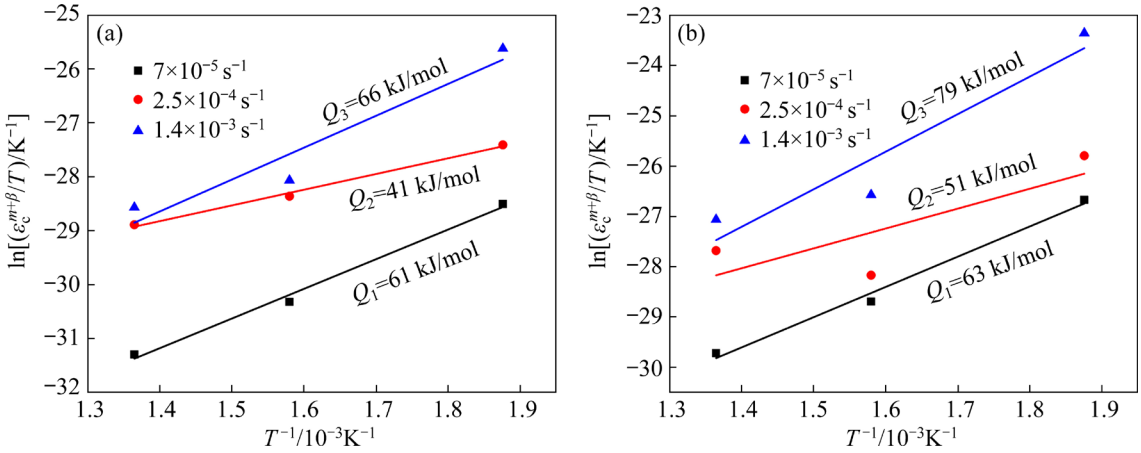

Fig. 8 $\ln(\varepsilon_c^{m+\beta}/T)$ versus $1/T$ plots at different tensile strain rates using Method II: (a) Before RHT; (b) After RHT

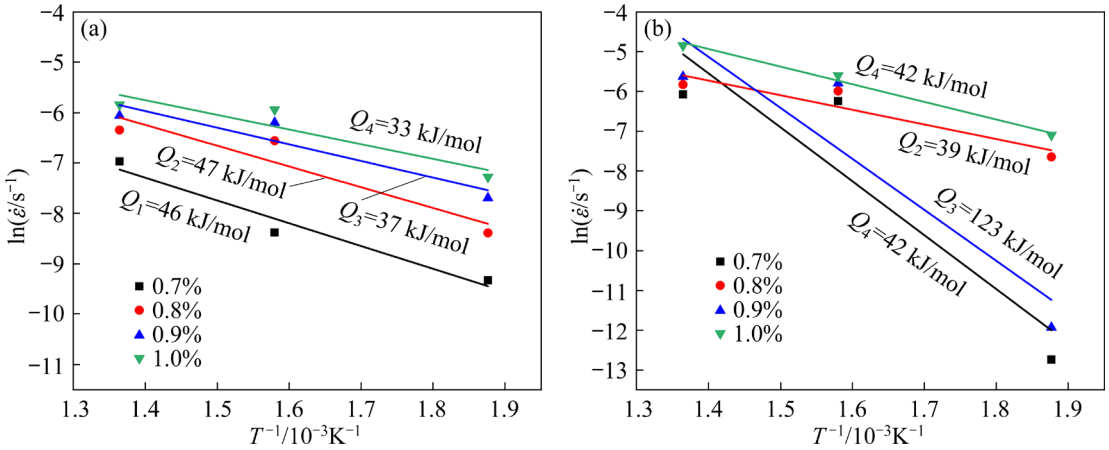

Fig. 9 $\ln\dot{\varepsilon}$ vs $1/T$ plots at different critical strains using Method III: (a) Before RHT; (b) After RHT

Fig. 5 with the curves of Fig. 5, including the extension lines. From Fig. 9(a), the Q values of the alloy before RHT were calculated to be 46, 47, 37, and 33 kJ/mol. From Fig. 9(b), the Q values of the alloy after RHT were 121, 39, 123, and 42 kJ/mol.

The $m+\beta$ and Q values obtained above are summarized in Table 5 along with their mean values.

Table 5 $m+\beta$ values, activation energies, and their mean values (values in brackets) of samples before and after RHT

Sample	$m+\beta$	Q/(kJ·mol^{-1})		
		Method I	Method II	Method III
Before RHT	4.3, 4.6, 3.7 (4.2)	78, 56, 81 (72)	61, 41, 66 (56)	46, 47, 37, 33 (41)
After RHT	2.9, 3.5, 3.2 (3.2)	71, 60, 90 (74)	63, 51, 79 (64)	121, 39, 123, 42 (81)

3.3 Microstructure evolution

3.3.1 Microstructure of alloy before and after RHT

The grain morphologies of the alloy before and after RHT are displayed in our previous work [30]. The grain boundaries of the alloy before RHT are coarse, and there are large grains and fine grain clusters (≤20 μm), with an average grain size of 54 μm. After RHT, the grain boundary of the alloy becomes finer, the fine grain clusters are significantly reduced, and the average grain size increases to 62 μm.

The effect of RHT on grain boundaries and precipitates was further investigated using SEM, as shown in Fig. 10. Figure 10(a) shows an SEM image of the alloy before RHT, showing the presence of a large number of precipitated phases at the grain boundaries and inside the grains, some of which precipitated along the grain boundaries and aggregated at the intersection position of the grain boundaries, leading to severe coarsening of the grain boundaries. Figure 10(b) shows the SEM

image of the alloy after RHT, indicating that the precipitated phases at the grain boundaries were dissolved, the agglomeration phenomenon disappeared, and the grain boundaries were clearly visible. However, a small amount of the precipitated phase remained inside the grains.

TEM was used to determine the type of the precipitated phase in Fig. 10, and the results are shown in Fig. 11. The precipitated phases were determined to be $M_{23}C_6$-type ($Mo_{23}C_6$) and MC-type (TiC) carbides based on the EDS and SAED analyses (Figs. 11(c) and (d)). The former is mainly distributed at the grain boundaries, whereas the latter is distributed both on the grain boundaries and within the grains. Figure 11(a) shows the morphology of $Mo_{23}C_6$ at the intersection position of grain boundaries with a length of approximately 600 nm. Figures 11(b) and (c) show the morphology

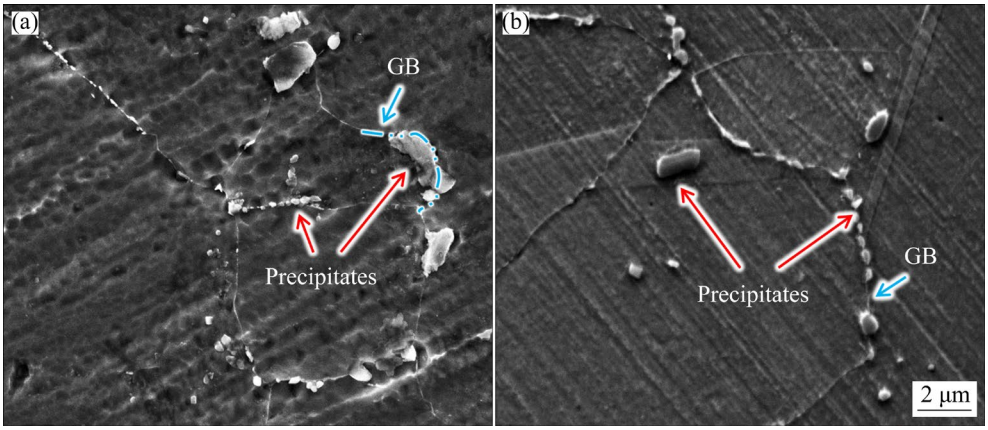

Fig. 10 SEM characterization results of precipitated phases: (a) Before RHT; (b) After RHT

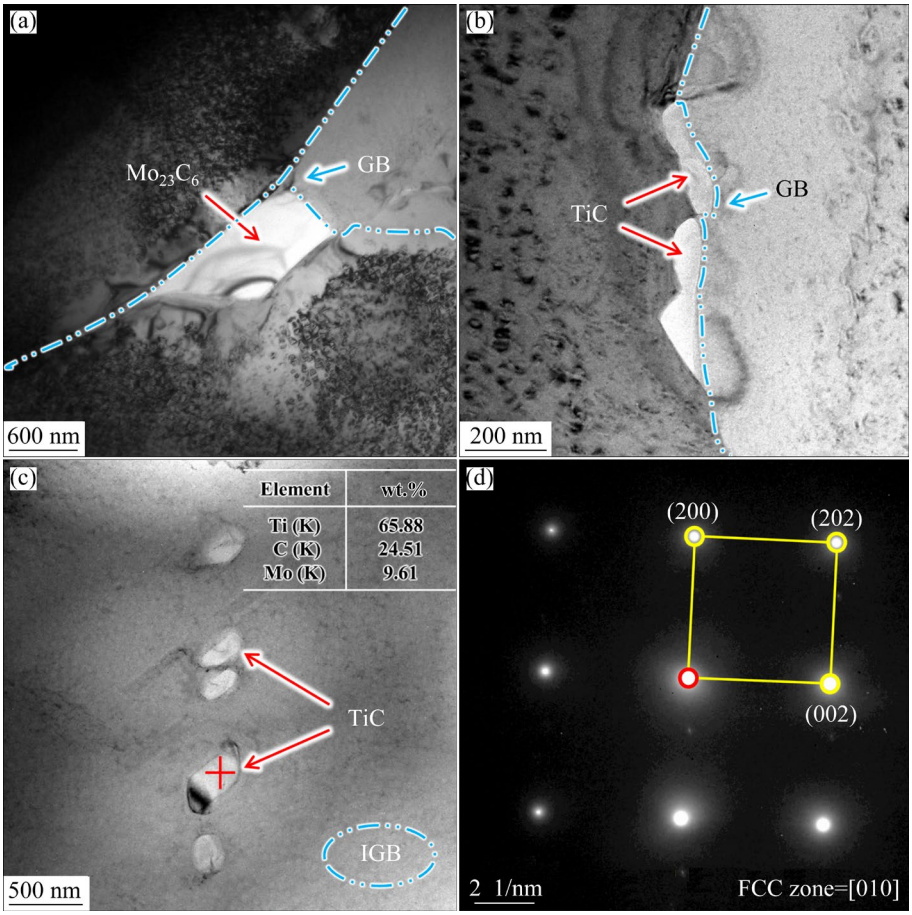

Fig. 11 TEM characterization results of carbides: (a) Morphology of $Mo_{23}C_6$; (b) Morphology of TiC at grain boundaries; (c) Morphology of TiC in grains and EDS results; (d) SAED results

of TiC at the grain boundaries and within a grain with a length of approximately 200 nm, respectively.

The precipitated phase of R26 alloy has a large amount of γ' phase in addition to carbides. Figure 12 shows the TEM characterization results of the γ' phase. From Fig. 12(a), it is evident that the dense γ' phase is distributed inside the grains and around the carbides. From Fig. 12(b), the γ' phase is a spherically precipitated phase with a diameter of about 50 nm. The characterization by EDS and SAED (Figs. 12(b) and (c)) shows that the matrix consists of γ phase, where the γ' phase has an FCC structure containing Ni, Co, Fe, Mo, Cr, and Ti.

Figure 13 shows the dislocations in specimens that were not subjected to tensile testing. As shown in Fig. 13(a), owing to the long service time of the selected R26 alloy, a large number of parallel dislocation lines existed in the alloy before RHT, and a high-density and entangled dislocation accumulated. Figure 13(b) shows that some γ' phases were cut by dislocations. After RHT, some of the dislocations in the alloy were eliminated, and the dislocation density was reduced.

3.3.2 Tensile fracture

Figure 14 shows the SEM characterization results of the tensile fracture at 23 °C. Before RHT, the fracture was mainly intergranular brittle rupture (Figs. 14(a) and (b). Figure 14(a) shows the blocky precipitated phases staggered along both sides of the crack. There were massive precipitated phases in the hole (Fig. 14(b)), and EDS showed that the precipitated phases were enriched with Ti and C. After RHT, both intergranular brittle rupture and transcrystalline rupture fracture characteristics were observed, as shown in Figs. 14(c) and (d). *Y*-type cracks and dimples are visible in Fig. 14(c), and there were precipitated phases in the center of the dimple. The EDS results of the precipitated phase in the dimple showed that the precipitated phase contained Ti, Ni, Mo, C, and other elements (Fig. 14(d)).

Figure 15 shows the SEM characterization results

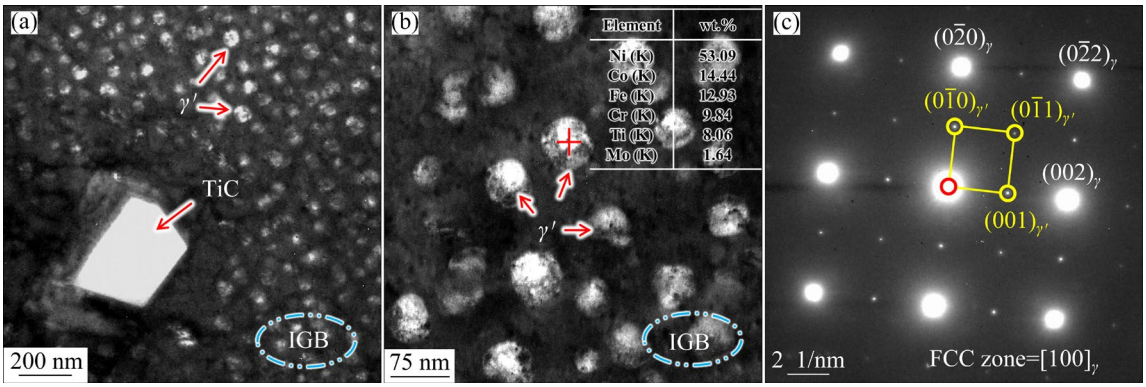

Fig. 12 TEM characterization results of γ' phase: (a) Positional relationship between TiC and γ' phase; (b) Morphology of γ' phase and EDS results; (c) SAED results

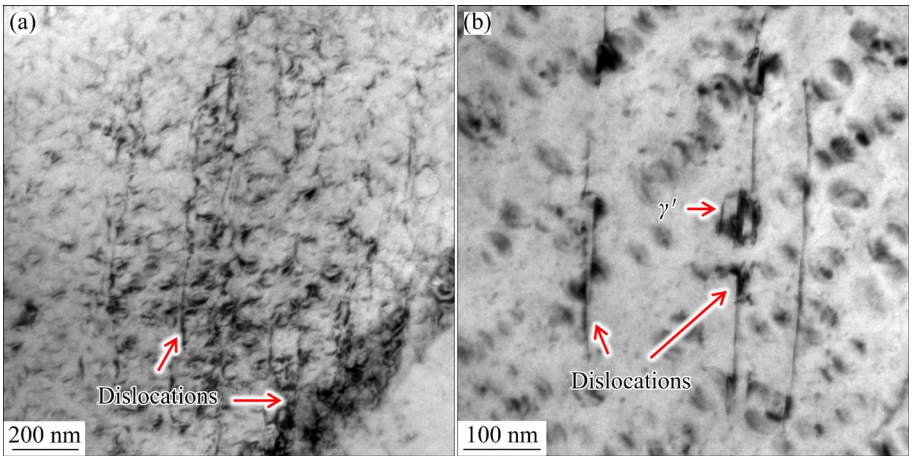

Fig. 13 TEM characterization results of dislocations in specimens without tensile testing: (a) Before RHT; (b) After RHT

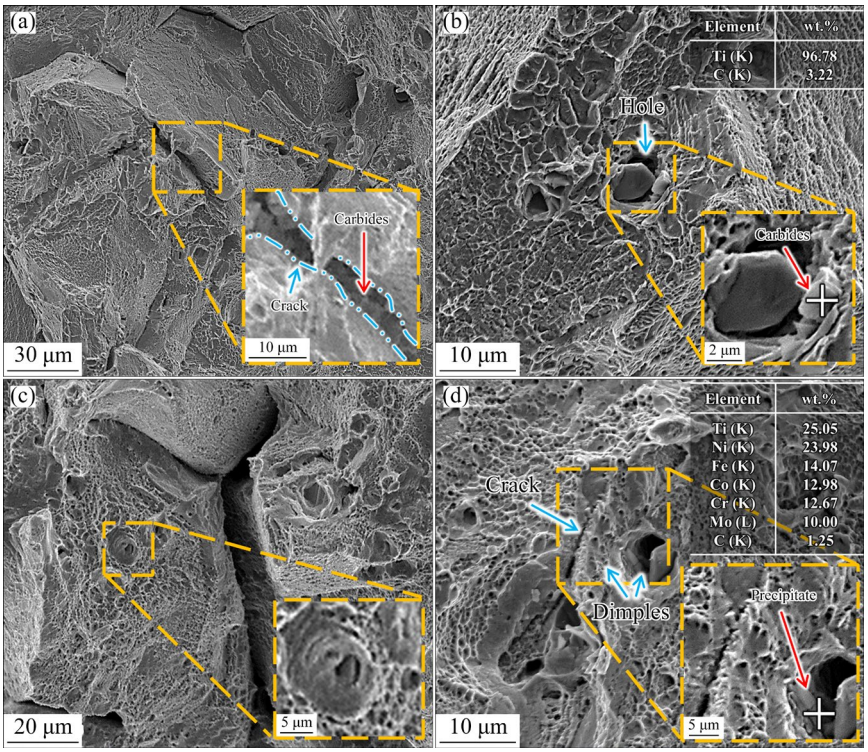

Fig. 14 SEM characterization results of tensile fracture at 23 °C: (a, b) Before RHT; (c, d) After RHT

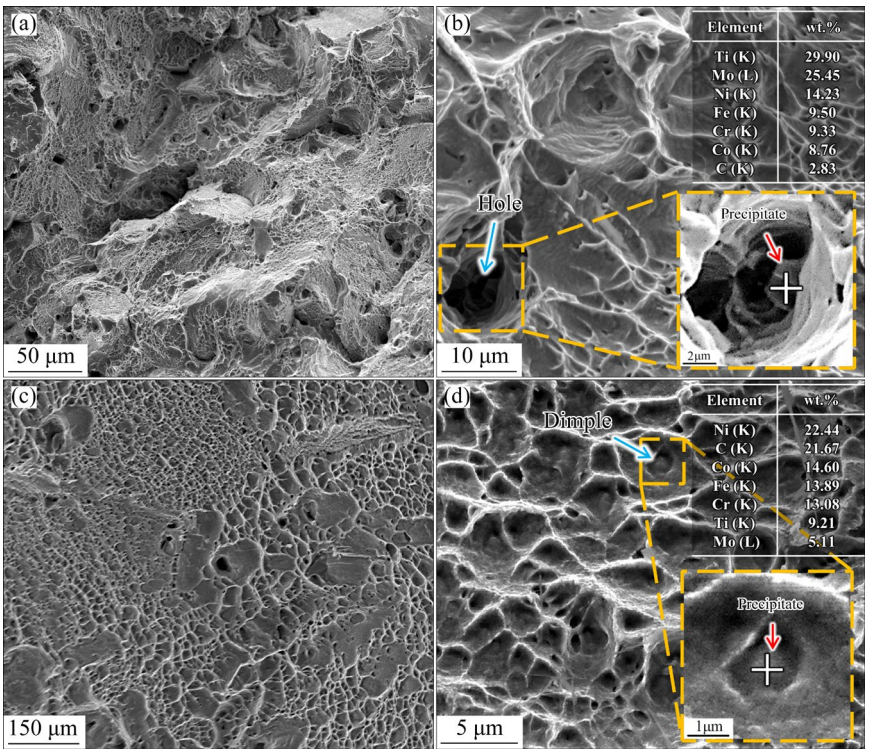

Fig. 15 SEM characterization results of tensile fracture at 560 °C: (a, b) Before RHT; (c, d) After RHT

of the tensile fracture at 560 °C. Before RHT, both intergranular brittle rupture and transcrystalline rupture fractures were observed in the fracture (Figs. 15(a) and (b)). Figure 15(a) shows the presence of flat intergranular fracture surfaces and hole in the fracture. Massive precipitated phases were observed in the hole (Fig. 15(b)). The EDS analysis showed that the precipitated phases contained elements such as Ti, Mo, Ni, and C. After RHT, the fracture was mainly transcrystalline

rupture (Figs. 15(c) and (d)). Dense dimples were distributed in the fractures (Fig. 15(c)). Figure 15(d) showed the presence of a spherical precipitate at the center of the dimple and the EDS results showed that the phase contained Ni, C, Co, Ti, and other elements.

4 Discussion

4.1 Causes of serrated flow

Figure 2 shows that the sawtooth flow phenomenon occurs in the R26 high-temperature alloy, and the sawtooth characteristics vary among specimens and with changes in tensile temperature. The four main types of serrations are Types A, A+B, B, and C. Type A typically occurs at lower tensile temperatures and has a stress level above the general curve. Type A+B or B occurs at moderate tensile temperatures, with a high frequency of sawtooth oscillations [31], and has a stress level either below or above the general curve. Type C occurs at higher tensile temperatures and has a stress level below the general curve. The evolution of sawtooth flow is related to the dynamic interaction between solute atoms and movable dislocations [32]. This interaction typically creates a short-range potential for dislocation motion. The diffusion of solute atoms in the matrix is briefly hindered by movable dislocations, which controls the evolution of solute concentration in the matrix through the effective pinning time [33]. The connection between moving dislocation and solute atoms can be expressed as [34]

$$\sigma_{\text{short}}=\xi C^{*} \tag{6}$$

where σ_{short} refers to the potential barrier in short ranges; ξ refers to the strength of solute atoms pinning to the moving dislocation; C^{*} refers to the concentration of solute atoms towards the moving dislocation line.

To study the fundamental mechanism of serrated flow, the variations in the critical strain with temperature and strain rate at the beginning of the serrated strain are shown in Fig. 5. Before and after RHT, the critical strains of the different alloys decreased with decreasing strain rate or increasing temperature, indicating that the alloys underwent a positive PLC phenomenon. In their study on DSA in Ni-based alloys, HALE et al [35] attributed DSA to the lattice and pipe diffusion of carbon atoms in the nickel matrix, with the lattice diffusion activation energy of carbon atoms in the nickel matrix being 139 kJ/mol. The activation energy of pipeline diffusion of solutes is 0.4−0.7 times the activation energy of lattice diffusion [36], i.e., the activation energy of pipeline diffusion of carbon atoms in nickel matrix is 56−97 kJ/mol. Table 5 shows that the average activation energies were calculated before and after RHT using the three methods as 41−72 kJ/mol and 64−81 kJ/mol, respectively. This is comparable to the activation energy for the duct diffusion of carbon atoms in the nickel matrix, from which it can be inferred that the cause of the serrated flow behavior of the R26 alloy is the duct diffusion of carbon atoms in the nickel matrix into the dislocation. The $m+\beta$ values are usually considered to correspond to different mechanisms leading to serrated flow, and the $m+\beta$ values should be in the range of 0.5−3. DSA in Ni-based alloys is attributed to interstitial solute diffusion when the value of $m+\beta$ is between 0.5 and 1. DSA in Ni-based alloys is attributed to alternative solute diffusion when the value of $m+\beta$ is between 2 and 3 [26]. However, in this study, the mean values of $m+\beta$ (4.2 and 3.2) are beyond the range of the specified solute diffusion mechanism, because the macroscopic tensile curve largely depends on the microstructure of the alloy [32,33]. β is an exponent related to the dislocation density (ρ_{m}) and has the following equation with respect to the true strain (ε):

$$\rho_{\text{m}} \propto \varepsilon^{\beta} \tag{7}$$

From Eq. (7), the value of β is positively correlated with the magnitude of dislocation density in the alloy organization. ROY et al [24] determined the dislocation density of C-276 alloy and obtained the β value. The special material used in this study, an R26 alloy with 6×10^{4} h of service, was selected. The alloy before RHT was damaged by service, and there were dislocations with high density (Fig. 13(a)); therefore, the calculated $m+\beta$ value was too large. Correspondingly, certain dislocations in the alloy disappeared after RHT, resulting in a decrease in dislocation density and $m+\beta$ value (Fig. 13(b)).

From the analysis of the stress drop and reloading time, the alloy after RHT showed a more obvious serrated flow phenomenon (Fig. 4). Figure 16 shows the evolution of the microstructure, fracture, and DSA of the R26 alloy before and after

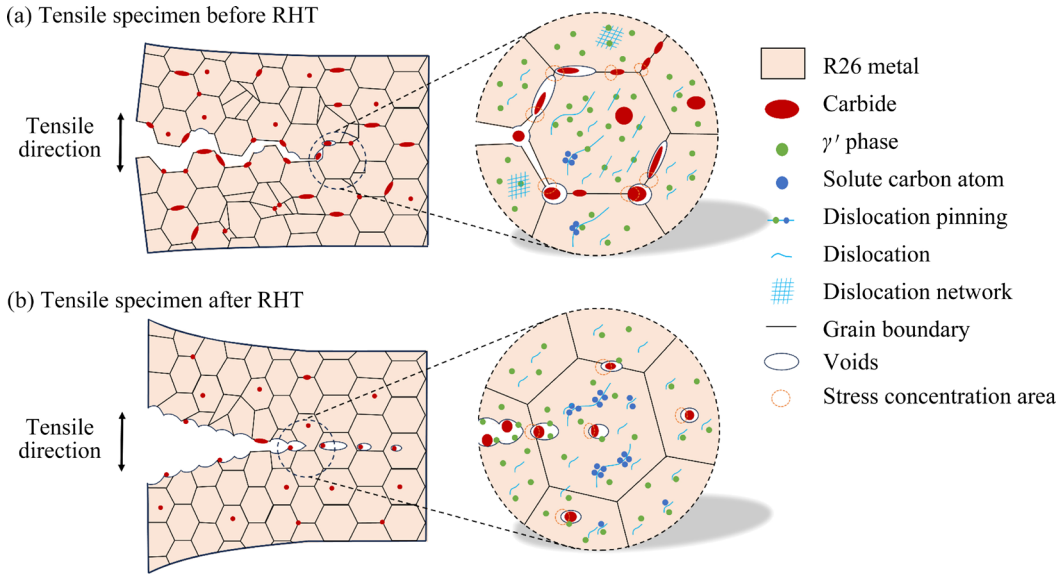

Fig. 16 Evolution of organization, fracture, and dynamic strain aging of R26 alloy before and after RHT

RHT. Combined with the solute pipe diffusion model [15], it is speculated that the R26 alloy after RHT showed a more obvious serrated flow phenomenon because of the higher concentration of carbon atom solutes in the matrix. Carbon atoms were mainly present in the matrix and precipitate phases (carbides) of the R26 alloy. A large number of carbides consisting of carbon atoms exist within the alloy before RHT, and only a small portion of the carbon atoms can participate in the DSA as a solute. RHT dissolves the carbides and releases a large number of carbon atoms into the matrix. More carbon atoms can participate in DSA and pin movable dislocations, so that it takes longer time for movable dislocations to accumulate more energy to unpin. Macroscopically, Fig. 4 showed a greater stress drop and longer reloading time, resulting in a more evident serrated strain curve.

4.2 Changes in properties, microstructure, and fracture mode

As described in Section 3.1, the hardness of the alloy after 6×10^4 h of service was beyond the standard range, and the alloy was less plastic and more brittle. On the one hand, this was due to the presence of fine grain clusters with a small average grain size in the alloy before RHT, and the smaller grain size implies an increase in the number of grain boundaries. During plastic deformation, the grain boundaries hinder the movement of dislocations, thus enhancing the deformation resistance of the material. On the other hand, this was due to the presence of a large amount of carbides on the grain boundaries of the alloy before RHT (Fig. 10(a)), and the grain boundaries were coarsened. Carbides were hardened phases with higher hardness than the alloy matrix. When carbides are present at the grain boundaries, they will further strengthen the grain boundary region and hinder dislocation glide and grain glide, thereby inhibiting plastic deformation. By contrast, the average grain size of the alloy increased after RHT and the grain boundary carbides dissolved (Fig. 10(b)), with a corresponding decrease in tensile strength and an increase in elongation.

The evolution of carbides (Fig. 10) affected the manner in which the alloy fractured. The plasticity of the alloy before RHT was poor. As shown in Figs. 14(a) and (b), massive carbides formed by Ti and C were found at the center of the cracks and holes of the tensile fracture at room temperature. By comparing Figs. 10(a) and 11, it is speculated that the carbide was TiC. This implies that when the alloy is stretched at room temperature before RHT, the source of cracking initiation is preferentially budded in TiC, which grows into cracks along the grain boundaries and gradually tears the grain boundaries to form fracture surfaces, ultimately leading to fracture. The number of dimples on the fracture surface of the alloy increased after RHT (Fig. 14(c)). From the EDS analysis of the precipitated phase in the center of the dimple in Fig. 14(d), combined with the position relationship between the γ' phase and the carbide in Fig. 12(a)

and the elemental composition analysis of the γ' phase, it was speculated that the precipitated phase was composed of carbide and γ' phase. This indicated that RHT dissolved some carbides at the grain boundary. At this point, the alloy no longer began to fracture from the grain boundaries. The generation positions of some crack-initiation sources were transferred to the precipitated phase clusters in the grains, and dimples were formed under tension.

When the temperature rises to 560 °C, the thermal motion of the metal atoms is enhanced, making the movement of dislocations in the crystals more likely [37], which can reduce the tensile strength of the alloys and enhance the elongation, which is reflected in Fig. 3. The effect of temperature increase on fracture was mainly to increase the number of fracture dimples. The precipitated phases in the dimples of the alloy before RHT were mainly composed of carbides and γ phases, and the fracture mode was intergranular and transcrystalline mixed fracture. After RHT, a large number of dimples appeared in the fracture of the alloy, which was characteristic of trans-crystalline ductile fractures [38]. The occurrence of transcrystalline fracture was because there were more carbides and γ' phases in the grains than at the grain boundary carbides. In the high temperature environment, dimples were more likely to be generated at the γ/γ' interface rather than grain boundaries. Finally, a crack was formed with the density of the dimples.

The evolution of the organization, fracture, and DSA of the R26 alloy before and after RHT is shown in Fig. 16, providing insights into the link between the fracture mode and the serrated flow behavior of the R26 alloy in terms of the evolution of the carbon elements. Before RHT, the carbon atoms were mainly concentrated in the carbides at the grain boundaries, the solute concentration of carbon atoms in the matrix was low, and the DSA and serrated flow behaviors were not obvious. At this time, the location of the crack initiation source was mainly concentrated at the grain boundary carbide, and the fracture occurred along the grain boundary. After RHT, the grain boundary carbides dissolved to release carbon atoms, and the large amount of carbon atom solute caused DSA and enhanced the serrated flow behavior. At this point the position of part of the crack initiation sources shifted to the precipitated phase clusters (carbide and γ' phases) within the grain, resulting in transcrystalline fracture. Therefore, to reduce the serrated flow phenomenon and simultaneously avoid brittle fracture, it is necessary to rationally distribute the number of carbides and the concentration of carbon atom solutes in the alloy.

5 Conclusions

(1) The activation energies of R26 alloy before and after RHT were calculated, yielding average values of 41−72 and 64−81 kJ/mol, respectively. This suggests that the DSA of R26 alloy was induced by the pipeline diffusion of carbon atoms into the dislocations in the nickel matrix. Higher concentrations of carbon atom solutes in the crystal enhance DSA and sawtooth flow behavior.

(2) Before RHT, cracks sprouted from the grain boundary carbides in the alloy during room-temperature stretching, expanding along the grain boundaries. After RHT, part of the carbides at the grain boundary dissolved, the initiation position of some cracks transferred to the precipitated phase group composed of intragranular carbides and γ' phase, and dimples were formed in the fracture.

(3) Before RHT, the alloy sprouted cracks and fractures at carbides enriched along the grain boundaries. At this time, there were fewer carbon atoms in the matrix that could participate in DSA as a solute, and the serrated flow was not obvious. After RHT, the carbide at the grain boundary dissolved and part of the cracking sources transferred to the precipitated phase group inside the grain boundary. The dissolved carbides in the matrix released a large number of carbon atoms to enhance DSA, making the serrated flow phenomenon more significant.

CRediT authorship contribution statement

Jia-jian WANG: Conceptualization, Formal analysis, Writing − Original draft, Visualization; **Zhe-wen HAN:** Resources, Investigation; **Zhi-chun WANG:** Resources, Methodology; **Bo PENG:** Resources, Methodology; **Yue ZUO:** Validation, Investigation; **Ju KANG:** Writing − Review & editing, Supervision, Project administration, Funding acquisition.

Declaration of competing interest

The authors declare that they have no known

competing financial interests or personal relationships that could have appeared to influence the work reported in this paper.

Data availability

All data included in this study are available upon request by contact with the corresponding author.

Acknowledgments

This work was financially supported by the National Natural Science Foundation of China (No. 52175286), and the Tribology Science Fund of State Key Laboratory of Tribology in Advanced Equipment, Tsinghua University, China (No. SKLTKF20B16).

References

[1] WU Bin, LIANG Jing-jing, ZHOU Yi-zhou, YANG Yan-hong, LI Jin-guo, SUN Xiao-feng. Influence of laser power on microstructure and tensile property of a new nickel-based superalloy designed for additive manufacturing [J]. Transactions of Nonferrous Metals Society of China, 2023, 33(4): 1124−1143.

[2] ZHAO Jiang, QUAN Guo-zheng, ZHANG Yu-qing, XIONG Wei. Distribution and evolution of low-energy twin boundary density in time−space domain during isothermal compression for Ni80A superalloy [J]. Transactions of Nonferrous Metals Society of China, 2023, 33(11): 3387−3405.

[3] XU Guo-hua, DUAN Ran, WANG Lei, LIU Yang, MENG Fan-qiang. Effect of compositional homogenization on hot workability of Ni-based GH4061 superalloy [J]. Transactions of Nonferrous Metals Society of China, 2023, 33(6): 1792−1802.

[4] JIANG He, YANG Jing, DONG Jian-xin, ZHANG Mai-cang, YAO Zhi-hao, XIE Xi-shan. Stress relaxation behavior comparison of typical nickel-base superalloys for fasteners [C]//Proceedings of the 9th International Symposium on Superalloy 718 & Derivatives: Energy, Aerospace, and Industrial Applications. Berlin: Springer International Publishing, 2018: 789−804.

[5] MOSHAYEDI H, MOATTARI M, AZIZPOUR K. Failure analysis of outer casing bolts of a 325 MW steam turbine [J]. Engineering Failure Analysis, 2019, 97: 189−200.

[6] ROWE R A, TAJYAR A, MUNTHER M, JOHANNS K E, ALLISON P G, MOMENI K, DAVAMI K. Nanoscale serration characteristics of additively manufactured superalloys [J]. Journal of Alloys and Compounds, 2021, 854: 156723.

[7] DUAN Peng, LIU Zong-de, GU Shu-chao, WANG Song. Evolution in microstructure and mechanical properties of Inconel 783 alloy bolts after long term high-temperature aging at 700 °C [J]. Metals, 2020, 10(11): 1440.

[8] MENG C, HU W, SANDLÖBES S, KORTE-KERZEL S K, GOTTSTEIN G. The effect of large plastic deformation on elevated temperature mechanical behavior of dynamic strain aging Al−Mg alloys [J]. Acta Materialia, 2019, 181: 67−77.

[9] GAN Yi, HU Li, SHI Lai-xin, CHEN Qiang, LI Ming-ao, XIANG Lin, ZHOU Tao. Effect of AlLi phase on deformation behavior and dynamic recrystallization of Mg−Li alloy during hot compression [J]. Transactions of Nonferrous Metals Society of China, 2023, 33(5): 1373−1384.

[10] LIU Xu-dong, FAN Jiang-kun, LI Kai-di, SONG Yue-lin, LIU De-gui, YUAN Rui-hao, WANG Jun, TANG Bin, KOU Hong-chao, LI Jin-shan. Serrated flow behavior and microstructure evolution of Inconel 625 superalloy during plane-strain compression with different strain rates [J]. Journal of Alloys and Compounds, 2021, 881: 160648.

[11] XU Jun, CAO Cheng-ming, GU Ping, PENG Liang-ming. Microstructures, tensile properties and serrated flow of $Al_xCrMnFeCoNi$ high entropy alloys [J]. Transactions of Nonferrous Metals Society of China, 2020, 30(3): 746−755.

[12] LIU Gang, WANG Cao, HAN Zhen-hua, MIAO Xin-lei, LIU Xin-wang, YANG Xin, WANG Zhi-jun, ZHANG Guo-jun. Serrated flow stress and nano-precipitation in $(CoCrFeNi)_{94}Ti_2Al_4$ high entropy alloy [J]. Intermetallics, 2022, 141: 107429.

[13] GENG Ying-xin, ZHANG Di, ZHANG Ji-shan, ZHUANG Lin-zhong. Zn/Cu regulated critical strain and serrated flow behavior in Al−Mg alloys [J]. Materials Science and Engineering: A, 2020, 795: 139991.

[14] AIT-AMOKHTAR A H, FRESSENGEAS C, BOUABDALLAH K. On the effects of the Mg content on the critical strain for the jerky flow of Al−Mg alloys [J]. Materials Science and Engineering: A, 2015, 631: 209−213.

[15] SLEESWYK A W. Slow strain-hardening of ingot iron [J]. Acta Metallurgica, 1958, 6(9): 598−603.

[16] HAYES R W, HAYES W C. On the mechanism of delayed discontinuous plastic flow in an age-hardened nickel alloy [J]. Acta Metallurgica, 1982, 30(7): 1295−1301.

[17] NALAWADE S A, SUNDARARAMAN M, KISHORE R, SHAH J G. The influence of aging on the serrated yielding phenomena in a nickel-base superalloy [J]. Scripta Materialia, 2008, 59(9): 991−994.

[18] MILLER M K, BABU S S, BURKE M G. Comparison of the phase compositions in Alloy 718 measured by atom probe tomography and predicted by thermodynamic calculations [J]. Materials Science and Engineering: A, 2002, 327(1): 84−88.

[19] MAX B, VIGUIER B, ANDRIEU E, CLOUE J M. A re-examination of the Portevin-Le Chatelier effect in alloy 718 in connection with oxidation-assisted intergranular cracking [J]. Metallurgical and Materials Transactions A, 2014, 45: 5431−5441.

[20] VENKADESAN S, PHANIRAJ C, SIVAPRASAD P V, RODRIGUEZ P. Activation energy for serrated flow in a 15Cr−5Ni Ti-modified austenitic stainless steel [J]. Acta Metallurgica et Materialia, 1992, 40(3): 569−580.

[21] FU J X, CAO C M, TONG W, HAO Y X, PENG L M. The tensile properties and serrated flow behavior of a thermomechanically treated CoCrFeNiMn high-entropy alloy [J]. Materials Science and Engineering: A, 2017, 690: 418−426.

[22] SHANKAR V, VALSAN M, RAO K B S, MANNAN S. L. Effects of temperature and strain rate on tensile properties and activation energy for dynamic strain aging in alloy 625 [J]. Metallurgical and Materials Transactions A, 2004, 35: 3129−3139.

[23] SAKTHIVEL T, LAHA K, NANDAGOPAL M, CHANDRAVATHI K S, PARAMESWARAN P, PANNEER SELVI S, MATHEW M D, MANNAN S K. Effect of temperature and strain rate on serrated flow behaviour of Hastelloy X [J]. Materials Science and Engineering: A, 2012, 534: 580−587.
[24] ROY A K, PAL J, MUKHOPADHYAY C. Dynamic strain ageing of an austenitic superalloy: Temperature and strain rate effects [J]. Materials Science and Engineering: A, 2008, 474(1/2): 363−370.
[25] QIAN K W, REED-HILL R E. A model for the flow stress and strain rate sensitivity of a substitutional alloy: Cu−3.1at.% Sn [J]. Acta Metallurgica, 1983, 31(1): 87−94.
[26] SCOTT H, GORDON R B. Precipitation-hardened alloys for gas-turbine service — I: Metallurgical considerations [J]. Transactions of the American Society of Mechanical Engineers, 1947, 69(6): 583−591.
[27] TANG Wen-shu, XIAO Jun-feng, LI Yong-jun, ZHANG Jiong, GAO Si-feng, NAN Qing. Effect of re-heat rejuvenation treatment on γ' microstructure of directionally solidified superalloy damaged by creep [J]. Acta Metallurgica Sinica, 2018, 55(5): 601−610.
[28] ZHANG Jing, ZHENG Yun-rong, FENG Qiang. Study on rejuvenation heat treatment of a directionally-solidified superalloy DZ125 damaged by creep [J]. Acta Metallurgica Sinica, 2016, 52(6): 717−726.
[29] MOGUCHEVA A, YUZBEKOVA D, KAIBYSHEV R, LEBEDKINA T, LEBYODKIN M. Effect of grain refinement on jerky flow in an Al−Mg−Sc alloy [J]. Metallurgical and Materials Transactions A, 2016, 47: 2093−2106.
[30] WANG Jia-jian, WANG Zhi-chun, HAN Zhe-wen, ZUO Yue, JIAO Xiang-dong, KANG Ju. Effect of rejuvenation heat treatment on the microstructure and stress relaxation behavior of nickel-based superalloy with excess hardness [J]. Materials Characterization, 2023, 204: 113189.
[31] LIN Y C, YANG Hui, CHEN Dong-dong, HE Dao-guang. Stacked auto-encoder network to predict tensile deformation behavior of a typical nickel-based superalloy considering Portevin–Le Chatelier effects [J]. Metals and Materials International, 2021, 27: 254−261.
[32] LIN Y C, YANG H, CHEN X M, CHEN D D. Influences of initial microstructures on Portevin-Le Chatelier effect and mechanical properties of a Ni−Fe−Cr−base superalloy [J]. Advanced Engineering Materials, 2018, 20(8): 1800234.
[33] LIN Y C, YANG H, HE D G, CHEN J. A physically-based model considering dislocation–solute atom dynamic interactions for a nickel-based superalloy at intermediate temperatures [J]. Materials & Design, 2019, 183: 108122.
[34] JIANG Hui-feng, ZHANG Qing-chuan, CHEN Xue-dong, CHEN Zhong-jia, JIANG Zhen-yu, WU Xiao-ping, FAN Jing-hong. Three types of Portevin–Le Chatelier effects: Experiment and modelling [J]. Acta Materialia, 2007, 55(7): 2219−2228.
[35] HALE C L, ROLLINGS W S, WEAVER M L. Activation energy calculations for discontinuous yielding in Inconel 718SPF [J]. Materials Science and Engineering: A, 2001, 300(1/2): 153−164.
[36] GUPTA C, CHAKRAVARTTY J K, WADEKAR S L, DUBEY J S. Effect of serrated flow on deformation behaviour of AISI 403 stainless steel [J]. Materials Science and Engineering: A, 2000, 292(1): 49−55.
[37] XIONG Xin-hong, QUAN Dun-miao, DAI Peng-dan, WANG Zhi-ping, ZHANG Qiao-xin, YUE Zhu-feng. Tensile behavior of nickel-base single-crystal superalloy DD6 [J]. Materials Science and Engineering: A, 2015, 636: 608−612.
[38] WAN Zhi-peng, HU Lian-xi, SUN Yu, WANG Tao, LI Zhao, ZHANG Yong. Effect of solution treatment on microstructure and tensile properties of a U720LI Ni-based superalloy [J]. Vacuum, 2018, 156: 248−255.

恢复热处理对镍基高温合金锯齿流变行为和断裂机制的影响

王家健[1]，韩哲文[2]，王智春[2]，彭 波[2]，左 月[3]，康 举[1,4,5]

1. 北京石油化工学院 机械工程学院，北京 102617；
2. 华北电力科学研究院有限责任公司，北京 100045；
3. 钢铁研究总院 焊接研究所，北京 100081；
4. 北京石油化工学院 氢能研究中心，北京 102617；
5. 清华大学 高端装备界面科学与技术全国重点实验室，北京 100084

摘 要：通过拉伸试验和显微组织表征研究了恢复热处理(RHT)对镍基高温合金(R26)锯齿流变行为和断裂方式的影响。计算获得 RHT 前后 R26 合金锯齿流变活化能分别为 41~72 和 64~81 kJ/mol。动态应变时效是由碳原子在镍基体中向位错通道扩散引起的。在 RHT 前，碳化物聚集在晶界，裂纹起源于这些碳化物并沿晶界扩展；RHT 溶解晶界上的碳化物，使启裂源转移到晶内沉淀相。RHT 增加了基体碳原子浓度，从而增强了动态应变时效和锯齿流变行为。

关键词：恢复热处理；镍基高温合金；锯齿流变行为：断裂；活化能

(Edited by Wei-ping CHEN)